LETTER

https://doi.org/10.1038/s41586-018-0336-3

Ferroelectric switching of a two-dimensional metal

Zaiyao Fei[1,5], Wenjin Zhao[1,5], Tauno A. Palomaki[1,5], Bosong Sun[1], Moira K. Miller[1], Zhiying Zhao[2,3], Jiaqiang Yan[2], Xiaodong Xu[1,4] & David H. Cobden[1]*

A ferroelectric is a material with a polar structure whose polarity can be reversed (switched) by applying an electric field[1,2]. In metals, itinerant electrons screen electrostatic forces between ions, which explains in part why polar metals are very rare[3–7]. Screening also excludes external electric fields, apparently ruling out the possibility of ferroelectric switching. However, in principle, a thin enough polar metal could be sufficiently penetrated by an electric field to have its polarity switched. Here we show that the topological semimetal WTe_2 provides an embodiment of this principle. Although monolayer WTe_2 is centro-symmetric and thus non-polar, the stacked bulk structure is polar. We find that two- or three-layer WTe_2 exhibits spontaneous out-of-plane electric polarization that can be switched using gate electrodes. We directly detect and quantify the polarization using graphene as an electric-field sensor[8]. Moreover, the polarization states can be differentiated by conductivity and the carrier density can be varied to modify the properties. The temperature at which polarization vanishes is above 350 kelvin, and even when WTe_2 is sandwiched between graphene layers it retains its switching capability at room temperature, demonstrating a robustness suitable for applications in combination with other two-dimensional materials[9–12].

A polar material contains an axis (referred to as the polar axis) along which the two opposite directions are distinguishable. This property is necessary for the existence of a spontaneous electric polarization. Of the 32 three-dimensional crystal classes, the ten that have a polar axis are known as the pyroelectrics, because heating them changes any electric polarization along this axis to produce a voltage. When Anderson and Blount introduced[3] the term 'ferroelectric metal' in 1965, they were referring to the possibility of polar structure appearing in certain metallic crystals upon cooling. However, they assumed that, even if such polar metals existed, the polarity would not be switchable. Definite cases of metals with polar structure have been identified only very recently[4–7].

Several ferroelectric insulators have been found to maintain ferroelectric characteristics in ultrathin films[13–17]. However, when materials with a layered structure are thinned towards the monolayer limit their properties often change qualitatively. This is illustrated by, for example: graphene, which becomes a two-dimensional Dirac metal[11,12]; MoS_2, which changes from an indirect- to a direct-gap semiconductor[10]; and CrI_3, which varies between being antiferromagnetic and ferromagnetic[9]. Another example is the topological semimetal WTe_2[18], which becomes either a two-dimensional topological insulator[19–22] or a superconductor at low temperatures in the monolayer limit, depending on the level of electrostatic doping. Here we focus on another aspect of WTe_2: the fact that it is a polar metal. Its three-dimensional (1T′) structure has a polar space group[7], $Pnm2_1$, and it remains metallic down to a thickness of three layers when undoped[23] and a monolayer when electrostatically doped[20]. We show here that as WTe_2 approaches this limit the polarity can be switched, making it effectively ferroelectric even when it is metallic in the plane.

The 1T′ structure (Fig. 1a) contains b–c mirror (M) and a–c glide (G) planes, so the polar axis, which must be parallel to both of them, is the c axis, perpendicular to the layers[7,18]. We apply an electric field along this axis using the device geometry indicated in Fig. 1b. An electrically contacted thin WTe_2 flake is sandwiched between two hexagonal boron nitride (h-BN) dielectric sheets, with thicknesses of d_t (top) and d_b (bottom). Above and below are gate electrodes, usually of few-layer graphene, to which voltages V_t and V_b are applied relative to the grounded WTe_2 (see Methods, Extended Data Fig. 1 and Extended Data Table 1 for device fabrication and characterization).

We define the applied electric field passing upwards through the layer, which will couple to out-of-plane polarization, as $E_\perp = (-V_t/d_t + V_b/d_b)/2$. When $E_\perp$ is swept up and down, in the conductance of trilayer (Fig. 1c) and bilayer (Fig. 1d) devices we observe bistability near $E_\perp = 0$, characteristic of ferroelectric switching, at all temperatures T from 4 K to above room temperature. No bistability is seen in monolayer WTe_2 (Fig. 1e), consistent with its structure having a centre of symmetry (Fig. 1e inset, red circles) and hence being non-polar; this symmetry also rules out instabilities involving charge injection into the h-BN. Nor is bistability seen in thicker crystals, including when one is used as a gate electrode (Extended Data Fig. 2). This, and the larger field required to switch the trilayer device than the bilayer device, can be explained by screening of $E_\perp$ on a length scale of nanometres.

We saw similar bistability in all bilayer devices (Extended Data Fig. 3). To prove that it is associated with out-of-plane electric polarization, we made devices in which the top gate is replaced by monolayer graphene, the conductivity of which is sensitive to the precise electric field E_t in the upper h-BN. In Fig. 2 we present measurements at a series of temperatures on such a bilayer WTe_2 device (B2) with four gold contacts to the top graphene (Fig. 2a; Extended Data Fig. 4). If the WTe_2 acts as a conducting sheet then it will screen out any electric field due to a voltage applied to the bottom gate. Indeed, Fig. 2b demonstrates that the conductance G_{gr} of the graphene depends only very weakly on V_b, except in a certain interval where it jumps between two states. The conductance of the WTe_2 is bistable in precisely the same interval (Extended Data Fig. 4). The two states must correspond to different values of E_t that can occur for exactly the same set of applied bias voltages. This implies the existence of two different vertical distributions of charge in the bilayer WTe_2. We deduce that sweeping the bottom gate changes $E_\perp$ (here $E_\perp = V_b/(2d_b)$ because $V_t = 0$), which at the ends of the hysteresis loop flips the polarization state (henceforth denoted by P↑ or P↓), changing E_t by an amount δE_t, and so changing G_{gr}.

We infer δE_t by applying a bias V_W to the WTe_2 and measuring the change $\delta V = d_t \delta E_t$ that is required to produce the same change in G_{gr} (Fig. 2c). For the simplified case of $d_t = d_b$ and all voltages at zero, the electrostatic potential profile is inverted between P↑ (red) and P↓ (green), as sketched in Fig. 2d, and the areal polarization density is $P \approx \varepsilon_0 \delta V$ (Methods), where ε_0 is the vacuum permittivity. At 20 K, this gives $P \approx 1 \times 10^4\ e$ per cm, which is equivalent to transferring about 2×10^{11} electrons per cm^2 between the two layers, a distance of about 0.7 nm. This is three orders of magnitude lower than the volume polarization density of around 0.2 C m^{-2} $\approx 10^{14}$ electrons per cm^2 in the classic ferroelectric[1] $BaTiO_3$. Combined with the micrometre-scale

[1]Department of Physics, University of Washington, Seattle, WA, USA. [2]Materials Science and Technology Division, Oak Ridge National Laboratory, Oak Ridge, TN, USA. [3]Department of Physics and Astronomy, University of Tennessee, Knoxville, TN, USA. [4]Department of Materials Science and Engineering, University of Washington, Seattle, WA, USA. [5]These authors contributed equally: Zaiyao Fei, Wenjin Zhao, Tauno A. Palomaki. *e-mail: cobden@uw.edu

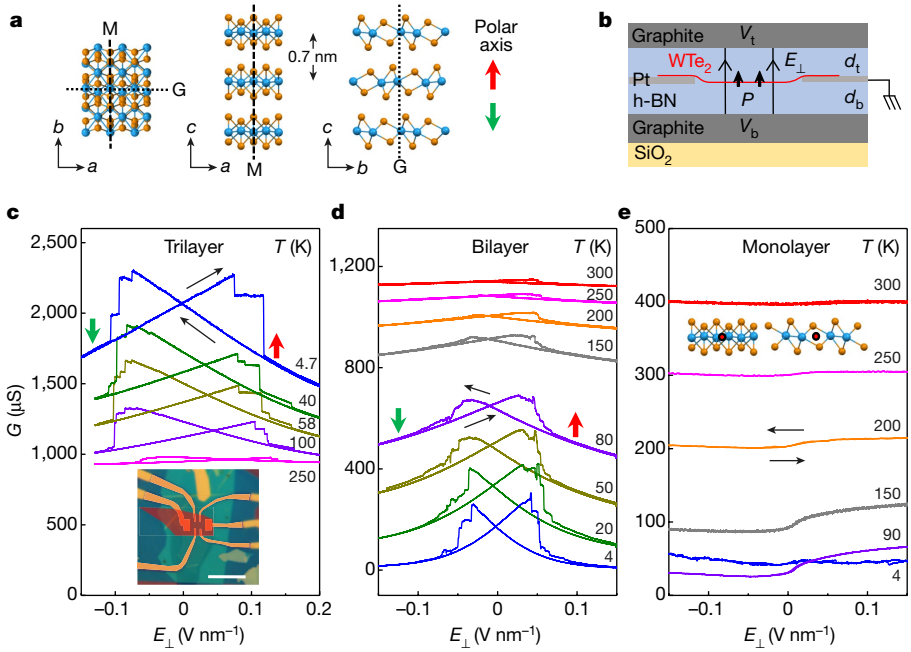

Fig. 1 | Evidence for ferroelectric switching in WTe_2. a, Structure of three-dimensional 1T′ WTe_2, showing the mirror plane (M; dashed), glide plane (G; dotted) and polar *c* axis (red arrow, up; green arrow, down). W atoms are blue; Te atoms are orange. **b**, Schematic cross-section of the device geometry used to apply an electric field $E_\perp$ normal to an atomically thin WTe_2 flake. **c**, **d**, Conductance *G* of undoped trilayer device T1 (**c**) and bilayer device B1 (**d**) as $E_\perp$ is swept up and down (black arrows), setting $V_t/d_t = -V_b/d_b$ to avoid net doping. The plots show bistability associated with electric polarization up (red arrow) or down (green arrow), at temperatures from 4 K to 300 K (as labelled). Here the conductance is the reciprocal of the four-terminal resistance. The undoped trilayer has a metallic temperature dependence, the bilayer an insulating one. Inset to **c**, optical image of a representative double-gated device. The WTe_2 flake has been artificially coloured red. Scale bar, 10 μm. **e**, Similar measurements on a monolayer WTe_2 device (M1), showing no bistability. At 4 K, conduction is in the quantum spin Hall regime. Insets, location (red circle) of a centre of symmetry in the monolayer, viewed along the *b* (left) and *a* (right) axes.

device size, such a small polarization makes it very hard to detect the ferroelectricity using standard displacement current measurements.

In Fig. 2e we plot δV as a function of *T*. Between about 60 K and 300 K it decreases roughly linearly with *T*, extrapolating to zero at roughly 450 K. However, above about 340 K the signal becomes unstable and we can no longer identify a hysteresis loop, suggesting that a transition to a non-polar state occurs in this temperature range.

We also made a simpler device with no top h-BN and monolayer graphene directly encapsulating the bilayer WTe_2. It exhibited highly reproducible hysteresis in the conductance, visible up to 300 K (Extended Data Fig. 5). This result demonstrates that the ferroelectric switching is robust enough for potential applications at room temperature that use it in combination with other two-dimensional materials.

We also investigated the effect of gate-induced charge doping, defined by $n_e = \varepsilon_{hBN}\varepsilon_0(V_t/d_t + V_b/d_b)/e$, where *e* is the electron charge and $\varepsilon_{h\text{-}BN}$ is the relative permittivity of h-BN. If the material were a simple metal, n_e would be the areal density of added electrons. In Fig. 3a, b we plot the conductance *G* at 7 K for device B1 (the same bilayer as in Fig. 1d), as a joint function of V_t and V_b, measured with V_t stepped and V_b swept up or down. Each sweep was started in the same fully polarized state. The black dashed lines in Fig. 3a, b denote $E_\perp = 0$ and the white dashed lines denote $n_e = 0$. The two plots differ only in the central hysteretic region, as is made clearer by plotting the difference between them (Fig. 3c). Similar behaviour is seen at higher temperature (Fig. 3d, at 200 K). At $E_\perp = 0$, *G* is a similar function of n_e for both P↑ and P↓ (Fig. 3e), with a temperature dependence that is insulating near $n_e = 0$ and metallic for $n_e > n_c$, with critical density $n_c \approx 2 \times 10^{12}$ cm^{-2}, as reported previously[20]. In Fig. 3f we show traces obtained by sweeping $E_\perp$ repeatedly up and down for selected values of n_e at 7 K. In each case the single conductance level at large $E_\perp$ evolves smoothly and reproducibly into one of the two stable levels as $E_\perp$ is reduced to zero, implying that the state remains uniformly polarized, without domain structure, at $E_\perp = 0$. For small or negative n_e, the effect of $E_\perp$ is large and of opposite sign for P↑ and P↓, producing butterfly-shaped hysteresis loops. For n_e well above n_c, $E_\perp$ has less effect on the conductance and the hysteresis is smaller, but still present. Hence, the doped bilayer device, like the trilayer device, is simultaneously ferroelectric and metallic.

At low temperatures (Fig. 3c) we observe an increase in the width of the hysteresis loop for increasingly negative n_e, whereas at 200 K (Fig. 3d) it is almost independent of n_e. When the conductance jumps there is some stochastic variation in the positions and substructure of the jumps, which is indicative of domain dynamics. If the surrounding gates were not present to screen the depolarization field, domains would inevitably form to limit the electrostatic energy[24], as observed in other ultrathin ferroelectrics[13,16,25,26]. In our devices, defects such as rips, bubbles and folds could nucleate domains or pin domain walls. In addition, $E_\perp$ is not completely uniform, because above and near the platinum contacts it is reduced by screening. Indeed, the pattern of switching depends on the choice of measurement contacts within a given device (Extended Data Fig. 6). We also observe that in some bilayer devices, such as B2 (Fig. 2), the switching field is not symmetric about $E_\perp = 0$. A possible explanation for this is that sometimes, despite all precautions, during device fabrication one side of the WTe_2 flake was exposed to mild oxidation, producing asymmetric trapped charge.

The fact that the conductance is sensitive to the polarization is consistent with the expectation that the polarization redistributes charge between the layers, which are inequivalent when $E_\perp$ is non-zero. Although the specific mechanisms for the sensitivity to n_e, $E_\perp$ and *P* are still under investigation, we remark on the following. First, the monolayer conductance at 4 K in Fig. 1e, which we know is due to edge conduction because this is the established quantum spin Hall regime, is almost independent of $E_\perp$. Second, in bilayers at large positive or negative n_e, the reversal of *P* has a similar effect on the conductance to that of changing $E_\perp$, changing it by approximately 0.15 V nm^{-1} at 7 K (indicated by the dotted horizontal line in Fig. 3f). This change in $E_\perp$ corresponds to a change in the electrostatic potential difference between the two WTe_2 layers by about 100 mV. This is of the same order

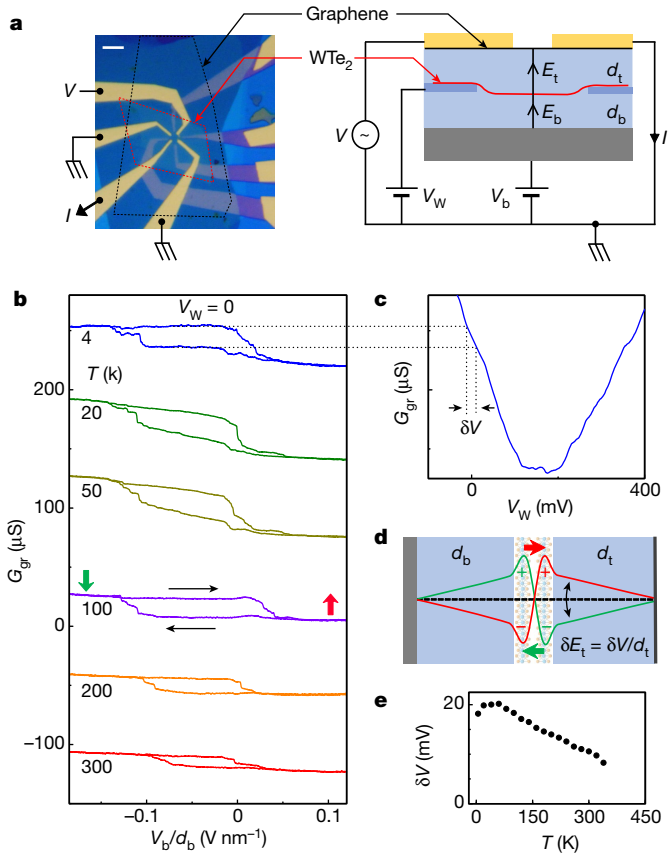

Fig. 2 | Detecting the out-of-plane polarization. a, Micrograph (left) and schematic cross-section (right) of a bilayer WTe_2 device (B2) with multiply contacted graphene in place of the top gate, indicating separately the electric fields in the h-BN above (E_t) and below (E_b) the WTe_2. Scale bar, 5 μm. **b**, The graphene conductance G_{gr} is measured when a bias V_b is applied to the bottom gate with the intervening WTe_2 grounded, at a series of temperatures (as labelled). The two conductance states seen for the two sweep directions (black arrows) are associated with different out-of-plane polarization states of the WTe_2 (red and green arrows as in Fig. 1). **c**, The behaviour of G_{gr} (the *y* axis is the same as in **b**) when a voltage V_W is applied directly to the WTe_2 provides a mapping to the difference $\delta E_t = \delta V/d_t$ in E_t between the two states. **d**, Sketch indicating how the reversal of the polarization changes the electrostatic potential (from red to green) and E_t (see text). **e**, Temperature dependence of δV, which is proportional to the polarization.

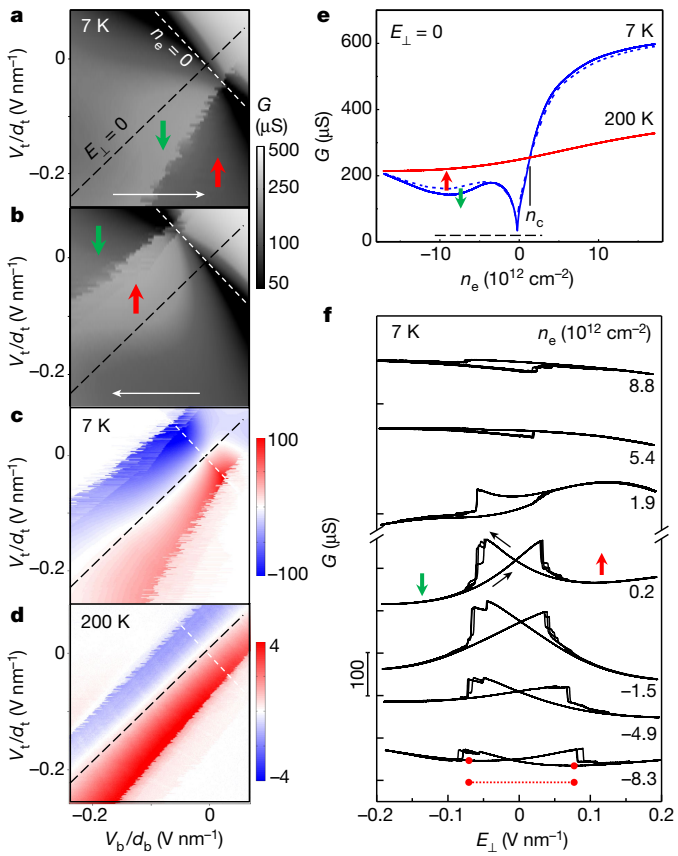

Fig. 3 | Gate tuning of the ferroelectric behaviour. a, **b**, Conductance *G* of bilayer device B1 at 7 K as a function of both gate voltages, for the two sweep directions of V_b as indicated by the white arrows. **c**, Difference between **a** and **b** at 7 K, which is non-zero in the hysteretic regime. **d**, Same measurement as in **c**, but at 200 K. In **a**–**d**, black and white dashed lines indicate contours of zero perpendicular field $E_\perp$ and zero charge density n_e, respectively. **e**, Variation in *G* with n_e at $E_\perp = 0$ for both polarization states (up, dashed; down, solid) at two temperatures (as labelled). The dashed bar near the bottom indicates the range of n_e in **a**–**d**, and n_c is the critical density (see text). **f**, Sweeps of $E_\perp$ for fixed n_e (as labelled) at 7 K. The dotted bar near the bottom indicates the magnitude of the approximate shift in $E_\perp$ of the conductance minimum between the opposite polarization states.

as the estimated change in the potential difference associated with the polarization reverse, $2\delta V \approx 40$ mV, suggesting that the potential imbalance between the layers governs the sensitivity of the conductance to both $E_\perp$ and *P*. It is also roughly the same as the width of the hysteresis loop; that is, the polarization flips roughly when the applied potential difference exceeds the potential due to the spontaneous polarization. This is another indicator that electron transfer between the layers may be involved. Third, the very sharp minimum seen in *G* close to $n_e = 0$ in bilayers (Fig. 3e) presumably marks the compensation point at which electron and hole densities are exactly equal, suggesting that electron–hole correlation may be important. Taken together, the above observations raise the possibility that electron–hole correlation effects, rather than a lattice instability[27], drive the spontaneous polarization in WTe_2. If this is the case, then the polarization could principally involve a relative motion of the electron cloud relative to the ion cores, rather than a lattice distortion, in which case the switching would be intrinsically very fast.

Ferroelectricity adds another ingredient to the intriguing combination of quantum spin Hall edges, correlation effects and superconductivity already seen in atomically thin WTe_2. Although the quantum spin Hall behaviour and superconductivity are restricted to the centro-symmetric monolayer and ferroelectricity occurs only for two or more layers, it is possible that these diverse phenomena are connected in ways that may also be relevant to understanding the properties that emerge in the three-dimensional limit, including extreme and anisotropic magnetoresistance[28,29], a polar axis and Weyl points[18,30].

Online content

Any Methods, including any statements of data availability and Nature Research reporting summaries, along with any additional references and Source Data files, are available in the online version of the paper at https://doi.org/10.1038/s41586-018-0336-3

Received: 14 February 2018; Accepted: 25 May 2018;
Published online 23 July 2018.

1. Dawber, M., Rabe, K. M. & Scott, J. F. Physics of thin-film ferroelectric oxides. *Rev. Mod. Phys.* **77**, 1083–1130 (2005).
2. Scott, J. F. Applications of modern ferroelectrics. *Science* **315**, 954–959 (2007).
3. Anderson, P. W. & Blount, E. I. Symmetry considerations on martensitic transformations: 'ferroelectric' metals? *Phys. Rev. Lett.* **14**, 217–219 (1965).
4. Shi, Y. et al. A ferroelectric-like structural transition in a metal. *Nat. Mater.* **12**, 1024–1027 (2013).
5. Benedek, N. A. & Birol, T. 'Ferroelectric' metals reexamined: fundamental mechanisms and design considerations for new materials. *J. Mater. Chem. C* **4**, 4000–4015 (2016).
6. Kim, T. H. et al. Polar metals by geometric design. *Nature* **533**, 68–72 (2016).

7. Sakai, H. et al. Critical enhancement of thermopower in a chemically tuned polar semimetal $MoTe_2$. *Sci. Adv.* **2**, e1601378 (2016).
8. Rajapitamahuni, A., Hoffman, J., Ahn, C. H. & Hong, X. Examining graphene field effect sensors for ferroelectric thin film studies. *Nano Lett.* **13**, 4374–4379 (2013).
9. Huang, B. et al. Layer-dependent ferromagnetism in a van der Waals crystal down to the monolayer limit. *Nature* **546**, 270–273 (2017).
10. Mak, K. F., Lee, C., Hone, J., Shan, J. & Heinz, T. F. Atomically thin MoS_2: a new direct-gap semiconductor. *Phys. Rev. Lett.* **105**, 136805 (2010).
11. Novoselov, K. S. et al. Two-dimensional gas of massless Dirac fermions in graphene. *Nature* **438**, 197–200 (2005).
12. Zhang, Y., Tan, Y. W., Stormer, H. L. & Kim, P. Experimental observation of the quantum Hall effect and Berry's phase in graphene. *Nature* **438**, 201–204 (2005).
13. Bune, A. V. et al. Two-dimensional ferroelectric films. *Nature* **391**, 874–877 (1998).
14. Martin, L. W. & Rappe, A. M. Thin-film ferroelectric materials and their applications. *Nat. Rev. Mater.* **2**, 16087 (2017).
15. Shirodkar, S. N. & Waghmare, U. V. Emergence of ferroelectricity at a metal-semiconductor transition in a 1T monolayer of MoS_2. *Phys. Rev. Lett.* **112**, 157601 (2014).
16. Liu, F. et al. Room-temperature ferroelectricity in $CuInP_2S_6$ ultrathin flakes. *Nat. Commun.* **7**, 12357 (2016).
17. Fei, R. X., Kang, W. & Yang, L. Ferroelectricity and phase transitions in monolayer group-IV monochalcogenides. *Phys. Rev. Lett.* **117**, 097601 (2016).
18. Soluyanov, A. A. et al. Type-II Weyl semimetals. *Nature* **527**, 495–498 (2015).
19. Qian, X., Liu, J., Fu, L. & Li, J. Quantum spin Hall effect in two-dimensional transition metal dichalcogenides. *Science* **346**, 1344–1347 (2014).
20. Fei, Z. et al. Edge conduction in monolayer WTe_2. *Nat. Phys.* **13**, 677–682 (2017).
21. Tang, S. et al. Quantum spin Hall state in monolayer 1T′-WTe_2. *Nat. Phys.* **13**, 683–687 (2017).
22. Wu, S. et al. Observation of the quantum spin Hall effect up to 100 kelvin in a monolayer crystal. *Science* **359**, 76–79 (2018).
23. Fatemi, V. et al. Magnetoresistance and quantum oscillations of an electrostatically tuned semimetal-to-metal transition in ultrathin WTe_2. *Phys. Rev. B* **95**, 041410(R) (2017).
24. Strukov, B. A. & Levanyuk, A. P. *Ferroelectric Phenomena in Crystals: Physical Foundations* 193–224 (Springer, Berlin, 1998).
25. Catalan, G., Seidel, J., Ramesh, R. & Scott, J. F. Domain wall nanoelectronics. *Rev. Mod. Phys.* **84**, 119–156 (2012).
26. Chang, K. et al. Discovery of robust in-plane ferroelectricity in atomic-thick SnTe. *Science* **353**, 274–278 (2016).
27. Cochran, W. Crystal stability and the theory of ferroelectricity. *Adv. Phys.* **9**, 387–423 (1960).
28. Ali, M. N. et al. Large, non-saturating magnetoresistance in WTe_2. *Nature* **514**, 205–208 (2014).
29. Zhao, Y. F. et al. Anisotropic magnetotransport and exotic longitudinal linear magnetoresistance in WTe_2 crystals. *Phys. Rev. B* **92**, 206803(R) (2015).
30. Wu, Y. et al. Observation of Fermi arcs in the type-II Weyl semimetal candidate WTe_2. *Phys. Rev. B* **94**, 121113 (2016).

Acknowledgements We thank J. Folk, E. Sajadi, A. Levanyuk, T. Birol and A. Andreev for substantial insights. D.H.C. and X.X. were supported by the US Department of Energy, Office of Basic Energy Sciences, Division of Materials Sciences and Engineering, under awards DE-SC0002197 and DE-SC0018171, respectively. Synthesis efforts at ORNL were also supported by the same division of the Department of Energy. Z.Z. was partially supported by the CEM, and NSF MRSEC, under grant DMR-1420451. T.A.P. was supported by AFOSR FA9550-14-1-0277. Z.F., W.Z. and B.S. were supported by the above awards and also by NSF EFRI 2DARE 1433496 and NSF MRSEC 1719797.

Reviewer information *Nature* thanks L. Bartels, T. Birol and the other anonymous reviewer(s) for their contribution to the peer review of this work.

Author contributions D.H.C. conceived the experiments; Z.Z. and J.Y. grew the crystals; W.Z., T.A.P., Z.F. and M.K.M. fabricated the devices; Z.F., W.Z., T.A.P. and B.S. performed the measurements; D.H.C., X.X., Z.F., W.Z. and T.A.P. analysed the results; and D.H.C., Z.F., T.A.P. and X.X. wrote the paper with comments from all authors.

Competing interests The authors declare no competing interests.

Additional information
Extended data is available for this paper at https://doi.org/10.1038/s41586-018-0336-3.
Reprints and permissions information is available at http://www.nature.com/reprints.
Correspondence and requests for materials should be addressed to D.H.C.
Publisher's note: Springer Nature remains neutral with regard to jurisdictional claims in published maps and institutional affiliations.

METHODS

Preparation and characterization of WTe_2 devices. We measured devices with four different layouts: (1) WTe_2 with graphite gates above and below (M1, B1, B4, T1); (2) bilayer WTe_2 with monolayer graphene as a top gate (B2); (3) a bilayer WTe_2/graphene heterostructure (B3); and (4) a monolayer graphene device gated by few-layer WTe_2 (F1). In the following, we describe fabrication of the first type; the others are similar.

First, graphite and h-BN crystals were mechanically exfoliated under ambient conditions onto substrates consisting of 285-nm thermal SiO_2 on highly p-doped silicon. Graphite flakes 2–6 nm thick were chosen for the top and bottom gates and 5–30-nm-thick h-BN flakes (a layered electrical insulator free of trapped charges and dangling bonds) were chosen for the top and bottom dielectric[31]. The top and bottom parts were prepared separately using a polymer-based dry transfer technique[32]. For the bottom part, an h-BN flake was picked up on a polymer stamp and placed on the bottom graphite. After dissolving the polymer, Pt metal contacts (about 8 nm) were patterned on the h-BN by standard e-beam lithography, e-beam evaporation and lift-off. For the top part, the top graphite was picked up first, then the top h-BN. Both stacks were then transferred to an oxygen- and water-free glovebox. WTe_2 crystals were exfoliated inside the glovebox and flakes from monolayer to trilayer thickness were optically identified and quickly picked up with the top part; the stack was then completed by transferring onto the lower contacts/h-BN/graphite stack before taking out of the glovebox. Finally, after dissolving the polymer, another step of e-beam lithography and metallization was used to define electrical bonding pads (Au/V) connecting to the metal contacts and the top and bottom gates. Extended Data Fig. 1 shows schematics of the fabrication processes and optical and atomic force microscope (AFM) images of a typical bilayer WTe_2 device (B4).

Estimate of the electric polarization. We use the following simplified model to estimate the spontaneous polarization of the bilayer WTe_2 from the measurements in Fig. 2b. We assume that $d_t = d_b \gg d$, where d is the thickness of the WTe_2, that all conductors (bottom graphite gate, top graphene and bilayer WTe_2) are grounded and have infinite electronic compressibility, and that the areal polarization density P is associated with two thin sheets of areal charge density $\pm P/d$ separated by d. Under these assumptions, when the polarization reverses there is no net flow of charge between the conductors and the WTe_2 remains neutral, and the potential profile between the gates is simply reversed when the polarization flips (Fig. 2d). By Gauss's law

$$\varepsilon_0\varepsilon_{hBN}E_t = \varepsilon_0 E_i + P/d \quad (1)$$

where E_t is the electric field in the h-BN (equal on both sides because the bilayer is neutral) and E_i is the field between the two charge sheets. Because the top graphene and the centre of the bilayer are both at zero potential,

$$2E_t d_t + E_i d = 0 \quad (2)$$

From equations (1) and (2):

$$E_t = \frac{P}{\varepsilon_0(2d_t + \varepsilon_{hBN}d)}$$

The change in E_t when the polarization reverses is then $\delta E_t = 2E_t = 2P/[\varepsilon_0(2d_t + \varepsilon_{hBN}d)]$. With $d_t \approx 10$ nm and $d \approx 1$ nm, the first term in the denominator dominates so $\delta E_t \approx P/(\varepsilon_0 d_t)$ and thus $P \approx \varepsilon_0 d_t \delta E_t = \varepsilon_0 \delta V$. In reality, d_b and d_t can differ by a factor of up to three, the conductors have finite compressibility and the polarization charge is more spread out, which taken together introduce an extra numerical coefficient of order unity.

Removing parallel (parasitic) conduction through the graphene in device B2. In device B2 the graphene extends over regions with no WTe_2 underneath so that it acts as a uniform gate for the entire WTe_2 sheet. The quantity that we call G_{gr} is the result of the following measurement, which maximizes sensitivity to only a central region of graphene above the WTe_2. First, we ground two opposing contacts to the graphene and measure only the current that flows from the biased contact to the one opposite, as shown in Fig. 2a. However, because of finite contact resistance, a small portion of this current still flows through graphene not above the WTe_2. To remove this parasitic current component, we set the WTe_2 voltage V_W such that the graphene is at its Dirac-point minimum in the region over the WTe_2. Because the minimum is quite broad, the graphene over the WTe_2 is then insensitive to V_b and the measured dependence on V_b comes from only the parasitic component, which can then be subtracted out. Note that removing it has no effect on the magnitude of the hysteresis.

In Extended Data Fig. 4b, we illustrate this procedure at 220 K. From the inset of Extended Data Fig. 4b, we determine that the graphene above the WTe_2 is at its Dirac point at $V_W = 129$ mV. The red curve shows the conductance of the graphene G_{gr} when $V_W = 129$ mV; the dependence on the back gate is from only the parasitic contribution. Conversely, in Fig. 2b and the blue curve in Extended Data Fig. 4b we measure G_{gr} at $V_W = 0$ mV, at which the graphene is most sensitive to changes in the electric field in the top h-BN E_t, yet also contains the parasitic conductance. The difference between these two curves (at $V_W = 129$ mV and $V_W = 0$ mV) is shown in black. The hysteresis remains, whereas the 'V' shape is mostly removed. The remaining small slope can be explained by the finiteness of the electronic compressibility of the bilayer WTe_2.

Using Extended Data Fig. 4b we can estimate the ratio of the parasitic current to that flowing above the WTe_2. The area with no WTe_2 has a h-BN thickness of $d_t + d_b = 33$ nm between the graphene and bottom gate. The red curve (with a parasitic V_b dependence) has a maximum slope of $dG_{gr}/dV_b = 17\ \mu S\ V^{-1}$ or $dG_{gr}/dE_t \approx 560\ \mu S\ V^{-1}$ nm after taking into account the h-BN thickness. From the inset curve, using voltage V_W applied to the WTe_2 for gating (with 8 nm h-BN) gives $dG_{gr}/dE_t = 12{,}300\ \mu S\ V^{-1}$ nm. Thus, the parasitic component is only about 5% of the total current.

Data availability. The data presented in this paper and that support the findings of this study are available from the corresponding author on reasonable request.

31. Dean, C. R. et al. Boron nitride substrates for high-quality graphene electronics. *Nat. Nanotechnol.* **5**, 722–726 (2010).
32. Zomer, P. J., Guimaraes, M. H. D., Brant, J. C., Tombros, N. & van Wees, B. J. Fast pick up technique for high quality heterostructures of bilayer graphene and hexagonal boron nitride. *Appl. Phys. Lett.* **105**, 013101 (2014).

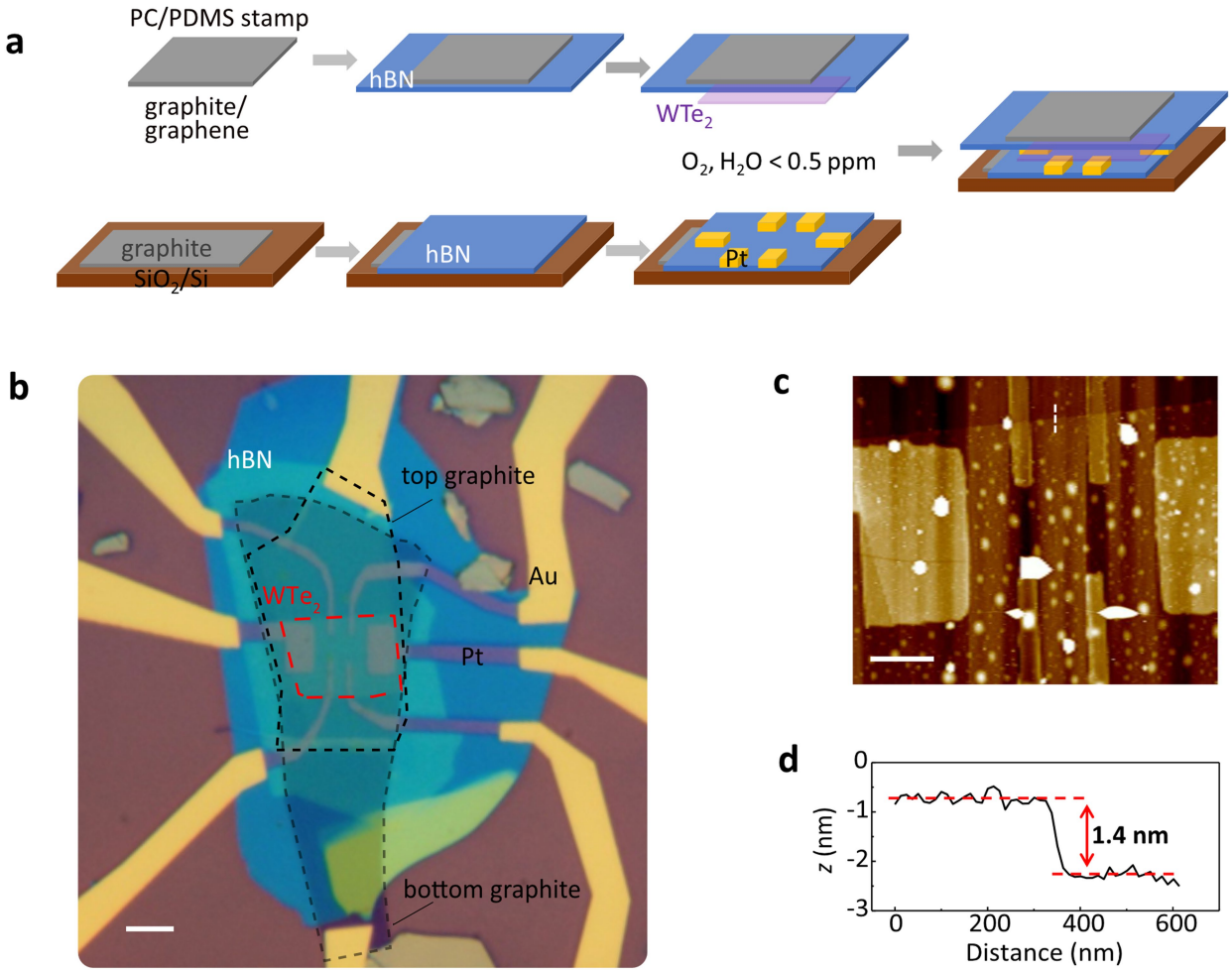

Extended Data Fig. 1 | Bilayer WTe_2 device. a, Essential steps in device fabrication. **b**, Optical image of device B4. The red dashed line outlines the bilayer flake. Scale bar, 5 μm. **c**, AFM topography image of the central region in **b**. Scale bar, 2 μm. **d**, Line cut along the white dashed line in **c**. The step height matches the expected bilayer thickness, about 1.4 nm.

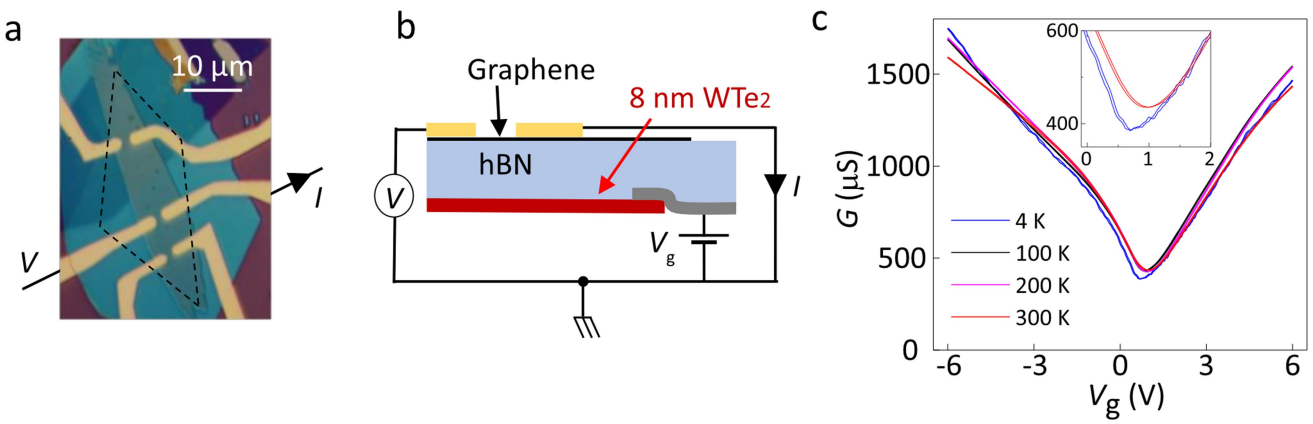

Extended Data Fig. 2 | Thick WTe_2 used as a gate. a, Optical image of device F1, in which a thick (8 nm) WTe_2 flake under 24-nm h-BN is used as a gate for a top graphene sheet. Scale bar, 10 μm. **b**, Schematic cross-section of the device. **c**, Two-terminal conductance G of the graphene as a function of voltage V_g applied to the WTe_2 flake. There is no sign of switching or bistability at any temperature, indicating that no polarization reversal occurs on the WTe_2 surface for fields of up to $E_\perp \approx 0.125$ V nm^{-1}. Inset, close-ups of the graphene Dirac point at 4 K and 300 K.

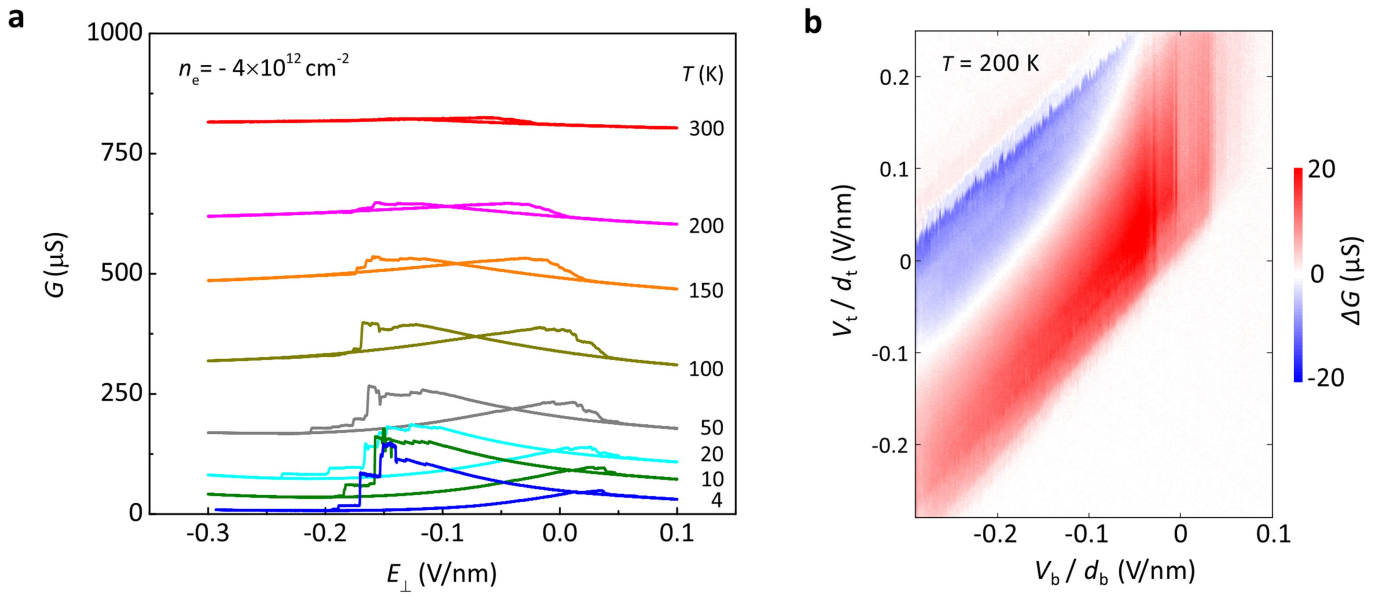

Extended Data Fig. 3 | Switching of an additional bilayer device. **a**, Conductance G versus perpendicular electric field $E_\perp$, at temperatures from 4 K to 300 K and a gate doping level of $n_e = -4 \times 10^{12}$ cm^{-2}, for device B4. **b**, Conductance difference ΔG between the two sweep directions of V_b at 200 K, as plotted in Fig. 3d for device B1.

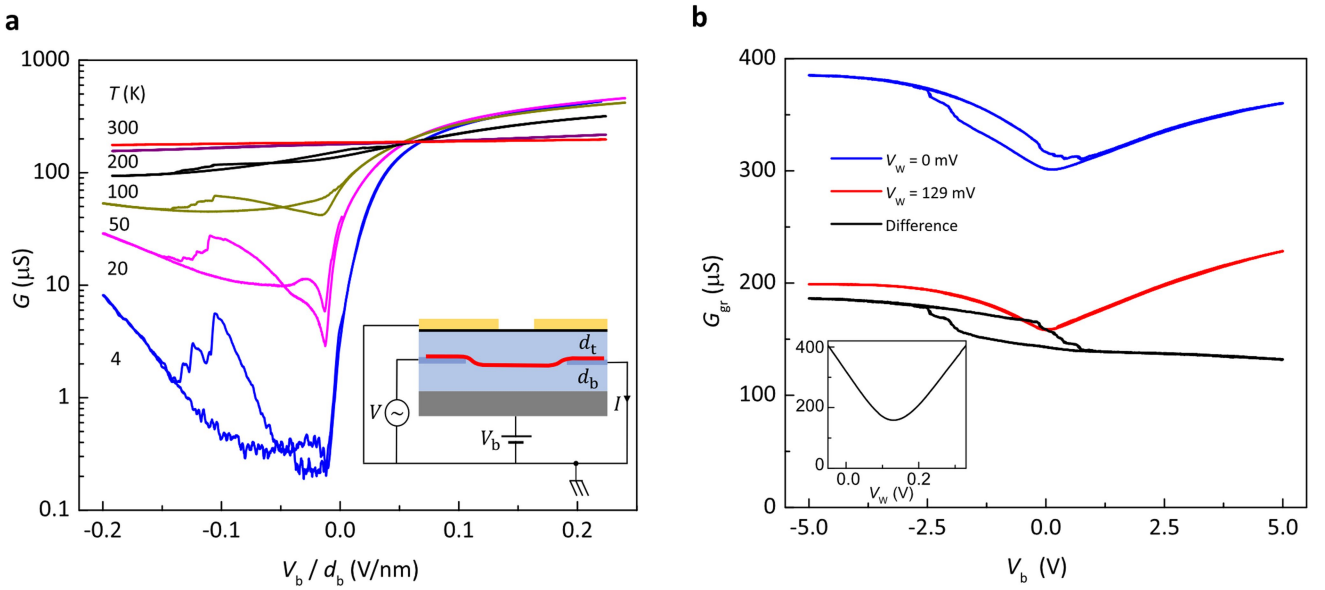

Extended Data Fig. 4 | Additional transport measurements and removal of parasitic effects in the polarization measurements. a, Conductance G versus V_b for the bilayer WTe_2 in device B2, measured with the top graphene grounded. The hysteresis occurs in exactly the same range of $E_\perp$ as it does in the graphene conductance in Fig. 2b. Note that both n_e and $E_\perp$ change when V_b is swept. The inset shows a schematic configuration of the measurement. **b**, Graphene conductance G_{gr} at 220 K as a function of V_b with the voltage V_W on the bilayer WTe_2 at 0 mV (blue) and 129 mV (red). The black curve is the difference between the blue and red curves. This subtraction removes most of the V_b dependence of the parasitic current that flows through the top graphene, which is not screened from the bottom gate by the WTe_2. Inset, graphene conductance showing the minimum at $V_W = 129$ mV.

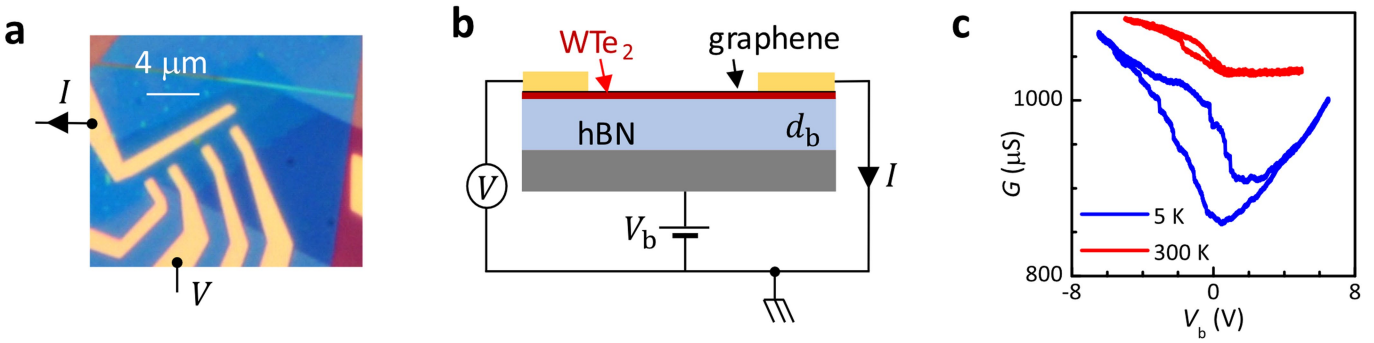

Extended Data Fig. 5 | Graphene/bilayer WTe_2 heterostructure showing hysteresis up to room temperature. a, **b**, Device image (**a**) and schematic cross-section (**b**). **c**, The two-terminal conductance *G* shows bistability at both 5 K and room temperature (300 K), implying that the polarization of the WTe_2 is still present in this hybrid structure.

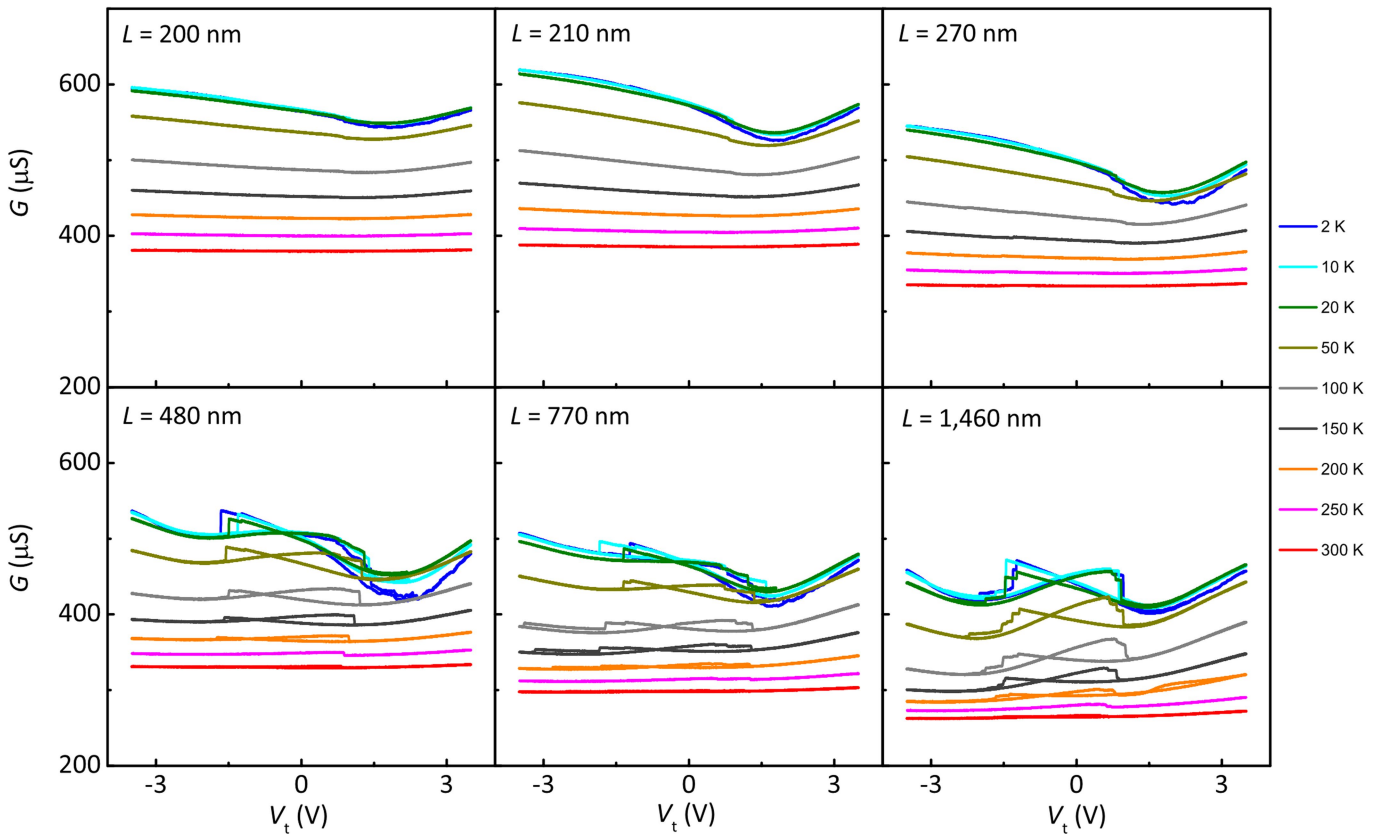

Extended Data Fig. 6 | Length-dependent ferroelectric behaviour in trilayer WTe_2 for temperatures from 2 K to 300 K. All measurements are performed at $V_b = 0$ in two-terminal configurations, where the contact separation ranges from 200 nm to 1,490 nm. For all devices mentioned above and in the main text, the contacts are separated by 1–2 μm. However, if we reduce the contact separation to a few hundred nanometers (270 nm), the metal contacts prevent the polarization from switching. For a contact separation (L) of more than 480 nm, the transfer characteristics show similar hysteric behaviour as in Fig. 1c, d and Extended Data Fig. 3a. Because V_b is always grounded, $E_\perp$ and n_e change simultaneously as we sweep V_t.

Extended Data Table 1 | Thickness of h-BN dielectrics and corresponding areal capacitances for the WTe_2 devices

Device label	WTe_2	top hBN (nm)	bottom hBN (nm)	C_t (1×10^{-3} F/m^2)	C_b (1×10^{-3} F/m^2)
M1	monolayer	6	28	5.9	1.3
B1	bilayer	12	20	3.0	1.8
B2	bilayer	8	25	4.4	1.4
B3	bilayer	NA	24	NA	1.5
B4	bilayer	10	21	3.5	1.7
T1	trilayer	5.5	23	6.4	1.1*
F1	8 nm	24	NA	1.5	NA

We define the gate-induced density imbalance to be $n_e = (C_tV_t + C_bV_b)/e$ and $E_\perp = (-C_tV_t + C_bV_b)/(2\varepsilon_{h\text{-}BN}\varepsilon_0)$, where the geometric areal capacitances are $C_t = \varepsilon_{hBN}\varepsilon_0/d_t$ and $C_b = \varepsilon_{hBN}\varepsilon_0/d_b$, $\varepsilon_{hBN} \approx 4$ is the dielectric constant of h-BN, and d_t and d_b are the thicknesses of the top and bottom h-BN flakes, respectively. All thicknesses were obtained from AFM images. In device B3, the WTe_2 flake is directly under the top graphene (no top h-BN). In device F1, the thick WTe_2 is directly on the bottom graphite (no bottom h-BN).
*For device T1, there is no bottom graphite; instead, we used the metallic silicon substrate as the bottom gate, the areal capacitance then being $C_b = \varepsilon_0/(d_b/\varepsilon_{hBN} + d_{SiO2}/\varepsilon_{SiO2})$. We did not make a four-layer device so we do not know at exactly what thickness polarization switching ceases to be possible.